JGR Space Physics

RESEARCH ARTICLE
10.1029/2023JA031644

Statistical Comparison of Various Dayside Magnetopause Reconnection X-Line Prediction Models

Ramiz A. Qudsi[1], Brian M. Walsh[1], Jeff Broll[2], Emil Atz[1], and Stein Haaland[3]

[1]Center for Space Physics, Boston University, Boston, MA, USA, [2]Los Alamos National Lab, Los Alamos, NM, USA, [3]The University Center in Svalbard, Longyearbyen, Norway

Key Points:

- Compared four different reconnection line models
- On average, the Maximum Bisection Field Model gives the best prediction of reconnection line location
- The Maximum Exhaust Velocity model gives the worst prediction of the reconnection line location

Correspondence to:

R. A. Qudsi,
qudsira@bu.edu

Citation:

Qudsi, R. A., Walsh, B. M., Broll, J., Atz, E., & Haaland, S. (2023). Statistical comparison of various dayside magnetopause reconnection X-line prediction models. *Journal of Geophysical Research: Space Physics*, *128*, e2023JA031644. https://doi.org/10.1029/2023JA031644

Received 25 APR 2023
Accepted 1 OCT 2023

Abstract Reconnection at Earth's magnetopause drives magnetospheric convection and provides mass and energy input into the magnetosphere/ionosphere system thereby driving the coupling between solar wind and terrestrial magnetosphere. Despite its importance, the factors governing the location of dayside magnetopause reconnection are not well understood. Though a few models can predict X-line locations reasonably well, the underlying physics is still unresolved. In this study we present results from a comparative analysis of 274 magnetic reconnection events as observed by the Magnetospheric Multiscale (MMS) mission to determine what quantities affect the accuracy of such models and are most strongly associated with the occurrence of dayside magnetopause reconnection. We also attempt to determine under what upstream solar wind conditions each global X-line model becomes least reliable.

Plain Language Summary Magnetic reconnection is an energy transferring process that happens at the Earth's magnetopause, the boundary between Earth's local plasma environment and the Sun's interplanetary environment. Reconnection helps move energy and particles into the region of space surrounding the earth called the magnetosphere. Dayside reconnection is important because it is a defining element to the amount of energy deposited into our magnetosphere. Despite its importance, scientists still do not completely understand how it works and where it happens. This study looks at many observations of magnetic reconnection to try and understand its precise location and figure out under which conditions it is more likely to occur. This paper compares in situ data with different models for predicting reconnection locations.

1. Introduction

The interplanetary magnetic field (IMF) emanating from the sun interacts with the terrestrial magnetic field giving rise to a complex and rich structures of scientifically interesting phenomena. The interaction between these two fields results in a reorientation of the topology of the magnetic field lines. This process is known as magnetic reconnection. The process is accompanied by the conversion of energy and is the primary process for exchange of particles between the solar wind and the magnetosphere (e.g., Paschmann, 2008). In three-dimensional space, the location of reconnection is a line known as X-line. Magnetic reconnection at Earth's magnetopause deposits energy into the terrestrial magnetic field, the results of which have important consequences for the shape, size, and dynamics of the magnetosphere.

In the classical picture of magnetic reconnection, ignoring the Earth's dipole tilt, reconnection occurs at the subsolar point when Earth's magnetic field lines encounter southward IMF, and in the polar cusp region for the northward IMF (Dungey, 1961). Southward IMF at the subsolar point, the point of the magnetosphere closest to the sun, results in a process called antiparallel reconnection since the Earth's magnetic field is in the Northward direction. On the other hand, for an arbitrary direction and magnitude of IMF, the location of reconnection is more complicated (Paschmann, 2008; Paschmann et al., 2013). Component reconnection occurs when the two reconnecting magnetic fields have some components of their directions perpendicular to the reconnection plane. Using in situ spacecraft data as well as simulation data, both anti parallel and component reconnection have been shown to occur at the magnetopause (Crooker, 1979; Fuselier et al., 2011; Gonzalez & Mozer, 1974; Paschmann et al., 1986, 2013, 2018; Trattner et al., 2007).

The location of reconnection sites, or X-lines, is crucial for understanding the dynamics of the magnetosphere and the effects of space weather at Earth. To predict the location of an X-line at the dayside magnetopause, multiple models have been developed over the last few decades. Some of these models encompass features of both antiparallel and component reconnection. A subset of these models suggests that reconnection occurs along a line

Table 1
A List of Reconnection Models, the Parameters Which Are Maximized and the Name Given to Those Models in This Study

Model no.	Reference	Parameter	Name
1	Moore (2002)	Reconnecting component	Maximum Bisection Field Model
2	Trattner et al. (2007)	Magnetic shear	Maximum Shear Model
3	Cassak and Shay (2007)	Hybrid Alfvén velocity	Maximum Exhaust Velocity Model
4	Hesse et al. (2013)	Reconnection energy	Maximum Reconnection Energy Model

or in a region where some physical quantity or a parameter is maximized. Table 1 lists four models compared in this study and the parameter which is maximized in each of the models. The fourth column lists the name of the corresponding model as has been used in this study.

One assumption in each of these models is that reconnection occurs as a single spatially extended X-line across the dayside magnetopause. Inherent in each of these models is a prediction for what underlying physics controls the location of reconnection at the interface between the shocked solar wind and magnetosphere. None of them have been rigorously tested against other models using simulation or in situ data. Komar et al. (2015) compared, among others, the models listed in Table 1 using global resistive magnetohydrodynamic (MHD) simulations and largely concluded that.

1. For the chosen [MHD] simulation parameters, we (Komar et al., 2015) find that all models are within a few Earth radii (R_E) of the magnetic separators when the IMF has a southward orientation and no dipole tilt.
2. None of the models chosen for this study faithfully reproduce the entire magnetic separators when the IMF has a northward orientation and no dipole tilt. However, only the maximum magnetic shear model faithfully reproduces the portion of the separator nightward of the magnetic nulls where reconnection is expected to occur.

For all the tested models, results were within a few Earth radii of the magnetic separators when the IMF had a southward orientation, but only the maximum magnetic shear model faithfully reproduced the portion of the separator nightward of the magnetic nulls when the IMF had a northward orientation. Komar et al. (2015) did not directly compare the models' outputs, nor was a statistical study done. Souza et al. (2017) compared the output from three different analytical models (Maximum Shear Model, Maximum Current Density Model, and Maximum Exhaust Velocity Model) with different spacecraft data. However, the study was done only for two reconnection events and thus lacked statistical significance. Nevertheless, several studies have validated the output of the Maximum Shear Model from different data sets (e.g., Fuselier et al., 2017; Petrinec et al., 2022; Trattner et al., 2021; Trattner, Burch, et al., 2017; Trattner, Thresher, et al., 2017). Another study was done recently by Liu et al. (2018) using a three-dimensional particle-in-cell simulations in which they compared the results, for companion 2D simulations, to different rate model predictions. Among the models that Liu et al. (2018) compared their predictions with, they found that for X-line orientation, the Maximum Reconnection Energy Model (or the Maximum Bisection Field Model, since the two are identical for a 2D case) provided the closest predictions.

Given the use of some of these models for mission designing and answering science questions (Fuselier et al., 2014), it is thus important to conduct a comparative study of these models using in situ spacecraft data for varying upstream solar wind conditions. In this study, we thus present a statistical comparison between four different dayside magnetopause reconnection X-line prediction models. The next section (Section 2) introduces and gives a brief overview of the four different X-line prediction models (listed in Table 1) considered in this study. Section 3 discusses all the data, both observation and simulation, used in this study as well as describes the methodology in detail. In the following section (Section 4), we present the results from the study and discuss the performance of the models for varying upstream solar wind conditions. Finally, Section 5 summarizes and concludes the study.

2. Science Background

There are several models in the literature that predict the location of the dayside magnetopause reconnection X-line. In this study we consider four such models (see Table 1) all of which have a common feature; they maximize a parameter along the magnetopause to find the location of the X-line. In this section, a brief overview of each model is presented to provide the necessary scientific background.

2.1. Maximum Shear Model

The Maximum Shear Model is an empirical model for the location of a reconnection X-line along the magnetopause surface based on the ion-flux distribution in the high-altitude cusps (Trattner et al., 2007). The model posits that reconnection "occurs along a ridge of maximum magnetic shear between the opposing magnetic fields on the two sides of the magnetopause" (Trattner et al., 2021). In order to find the location of the X-line, the maximum of the shear angle between the two opposing fields is found which is given as:

$$\cos(\theta) = \left(\mathbf{B}_{\mathrm{sh}} \cdot \mathbf{B}_{\mathrm{msp}}\right) / \left(|\mathbf{B}_{\mathrm{sh}}||\mathbf{B}_{\mathrm{msp}}|\right) \tag{1}$$

where $\mathbf{B}_*$ is the magnetic field and "sh" and "msp" refers to the magnetosheath and magnetosphere, respectively. Sections 3.1 and 3.2 describe in detail how the relevant data for each side is obtained.

Though the original Maximum Shear Model study only considered southward IMF conditions (Trattner et al., 2007), a more recent study has shown the model to be valid for northward IMF conditions as well without losing statistical accuracy as long as B_y is the dominant component (Trattner, Thresher, et al., 2017). Since its inception, several studies in literature have quantified the performance of Maximum Shear Model (Fuselier et al., 2017; Komar et al., 2015; Trattner, Burch, et al., 2017).

2.2. Maximum Reconnection Energy

The Maximum Reconnection Energy Model is a theoretical model proposed by Hesse et al. (2013) to describe the collisionless magnetic reconnection of asymmetric systems. The model suggests that in an asymmetric system, the magnetic reconnection line is oriented in such a way that the product of available magnetic energy is maximized. For magnetosphere and solar wind magnetic interactions the following parameter is maximized:

$$E \propto \left(|\mathbf{B}_{\mathrm{sh}}|^2 \times |\mathbf{B}_{\mathrm{msp}}|^2\right) \tag{2}$$

where E is proportional to the available energy from two available fields. The model was originally proposed and supported by small scale reconnection simulations and has been tested using an MHD simulation. Komar et al. (2015) compared several dayside magnetic reconnection models in global magnetosphere simulations, one of which was the Maximum Reconnection Energy Model and found that the Maximum Reconnection Energy Model was within a few Earth radii (R_E) of the X-line for southward IMF and no dipole tilt. The model is strictly two dimensional and to enhance confidence in the model, a full three-dimensional treatment of the theory is required.

2.3. Maximum Exhaust Velocity

The Maximum Exhaust Velocity Model is an application of a model proposed by Cassak and Shay (2007). The model conjectures that the X-line orientation is determined by maximizing the asymmetric reconnection outflow speed which is described as:

$$V_A \sim \left[\frac{B_{\mathrm{sh}} B_{\mathrm{msp}}\left(B_{\mathrm{sh}} + B_{\mathrm{msp}}\right)}{\left(n_{\mathrm{i,msp}} B_{\mathrm{sh}} + n_{\mathrm{i,sh}} B_{\mathrm{msp}}\right)}\right]^{1/2} \tag{3}$$

where $n_{\mathrm{i,msp}}$ and $n_{\mathrm{i,sh}}$ refers to the ion density in magnetosphere and magnetosheath, respectively. The predictions of this model have been found to be consistent with spacecraft observations of reconnection poleward of the cusp (Muzamil et al., 2014) as well as observations in simulations (Cassak & Fuselier, 2016; Komar et al., 2015). One of the limitations of the model is that it ignores the importance of plasma velocity parallel to the direction of reconnecting magnetic field (Komar et al., 2015).

2.4. Maximum Bisection Field

The Maximum Bisection Field Model was proposed by Moore (2002) to predict the location of the dayside X-line along the locus of points where the two opposing field lines, magnetospheric and magnetosheath, are bisected. This simplifies to finding the location where the following field is maximized:

$$B_{\text{rec}} = |\mathbf{B}_{\text{msp}} \cdot \mathbf{i}_{\text{xn}}| \tag{4}$$

where B_{rec} is the field component to be maximized and $\mathbf{i}$ is the unit vector normal to the X-line. If the slope of the reconnection line were m, then the slope of the unit vector $\mathbf{i}_{\text{xn}}$ will be $-1/m$. Once the location of the maximum reconnecting field is found, the X-line is then found by integrating away from the point along the bisector of angle between the local fields.

Moore (2002), using modeled data, assumes a perfect 1D rotational discontinuity therefore requiring a perfect magnetic balance between the magnetosheath and magnetospheric fields. This assumption in Moore (2002) is realized by setting the magnetosheath field equal to the magnetospheric field. In the current study, using in situ spacecraft data, we relax this assumption, instead assume that the balance is achieved by a combination of all field components and ram pressure. Stated in other words, the application of the Moore (2002) model is modified slightly to incorporate use of realistic magnetic field values.

For the 2D case, this direction is identical to the direction along which the proportional available magnetic energy is maximized as given by the Maximum Reconnection Energy Model (Hesse et al., 2013). This means that maximizing either Equation 2 or Equation 4 should give identical results. However, as seen in Section 4, for a full 3D case, though the output from the two models looks very similar (see the right panels in Figure 4), the location of the X-line as computed by maximizing each of the two parameters is slightly different results (see Tables 3 and 4).

Figure 1 shows the distribution of each of the four parameters discussed in this section, projected on the yz-plane. The parameters have been normalized against their respective maximum values. The three rows correspond to three different IMF conditions (shown at the top right of each plot). Top row corresponds to a purely southward IMF whereas the bottom row corresponds to purely northward IMF. Middle row shows the distribution for Parker spiral like condition with zero field in z direction. Clock angle for each IMF is shown in top left corner. For these sample plots, the ion density (n_{p}) is assumed to be 5 cm^{-3} with plasma bulk velocity of -500 km/s in the x direction and an average ion temperature of 1.5×10^{-6} K. The DST index is -5 nT and the dynamic pressure is 2.4 nPa. For simplicity, Earth's dipole tilt was assumed to be zero for all three cases. The magnetic fields were computed using the Tsyganenko-96 model (Tsyganenko, 1996). See Section 3.2 for more details on how these images were generated. These figures are similar to those reported in literature (Moore, 2002; Trattner et al., 2007).

3. Data Selection and Methodology

3.1. Data

This investigation uses high-resolution OMNI data (1 min resolution) propagated to the nose of Earth's bow shock (King & Papitashvili, 2005) along with data from the Fast Plasma Instrument (FPI) (Pollock et al., 2016) and the Fluxgate Magnetometer (FGM) (Russell et al., 2016; Torbert et al., 2016) aboard the MMS spacecraft. Since MMS is a constellation of four spacecraft, we looked into differences in the output of the model while using data from different spacecraft. We observed that using data from one versus another spacecraft made insignificant changes to the overall result of this study, and thus decided to use data from MMS 3 for this study. For easy identification of jet-reversal (see Section 3.2 for more details), the study uses high-resolution burst data from FPI which gives a full space density measurement every 150 ms (for ions). Section 3.2 describes how each of these data were used in this study and the methodology in greater detail.

3.2. Methodology

With the MMS spacecraft, between September 2015 and April 2018, 16,782 magnetopause current sheet crossings have been identified and documented (see Haaland et al. (2020) and Paschmann et al. (2018) for details of methodology used for identification and classification). A spacecraft crossing the magnetopause current sheet can observe enhanced ion velocity tangential to the current sheet. This enhancement, known as a reconnection jet, is an indication that reconnection is occurring nearby. Enhanced ion velocities with switching directions are called jet reversals, and are evidence of an X-line nearby the spacecraft position (e.g., Cowley, 1982; Dunlop et al., 2011; Gosling et al., 1982; Paschmann et al., 1979; Petrinec et al., 2022; Pu et al., 2007; Trattner, Burch, et al., 2017).

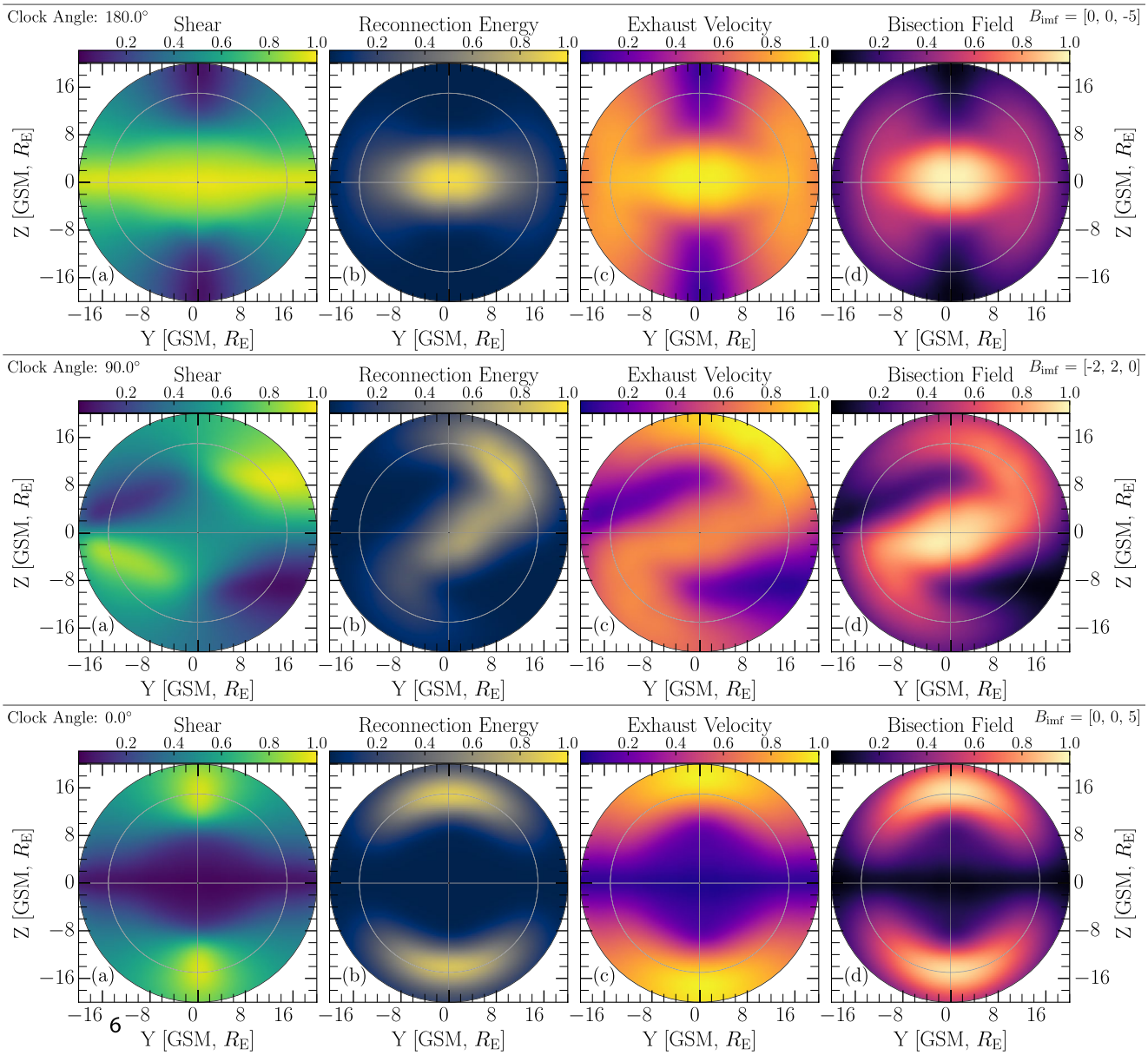

Figure 1. Sample figure of distribution of four parameters discussed in Section 2, projected on the *yz*-plane. Three rows correspond to three different interplanetary magnetic field (IMF) conditions (from top to bottom, purely southward IMF, Parker spiral and purely northward IMF) shown in the top right corner of each panel. For simplicity, Earth's dipole tilt is assumed to be zero.

For each identified crossing, we record a 10-min long time series centered at the crossing time (t_{cross}). We transform the magnetic field and the ion velocity from GSM-coordinate (Geocentric Solar Magnetic) to a local LMN-coordinate (boundary-normal) system using the empirical magnetopause model described in Shue et al. (1998). In the code, this was implement using coordinate transformation tools available in PySPEDAS (Grimes et al., 2019). Using the ion properties (density, temperature, and energy spectra), we identify the magnetosheath and magnetopause locations. If there are multiple crossings within the 10-min time period, then the values during the longest interval for both locations are averaged over to get a representative value of each parameter in that region. In the next step, we identify if a jet-reversal was observed by MMS during the crossing by inspecting the ion velocity directions. In order to minimize the impact of varying conditions for the magnetosheath because of changes in the upstream solar wind condition, we subtract the representative ion velocity, $\langle V_L \rangle$ of magnetosheath from the velocity time series and call the resultant parameter ΔV_L, defined as:

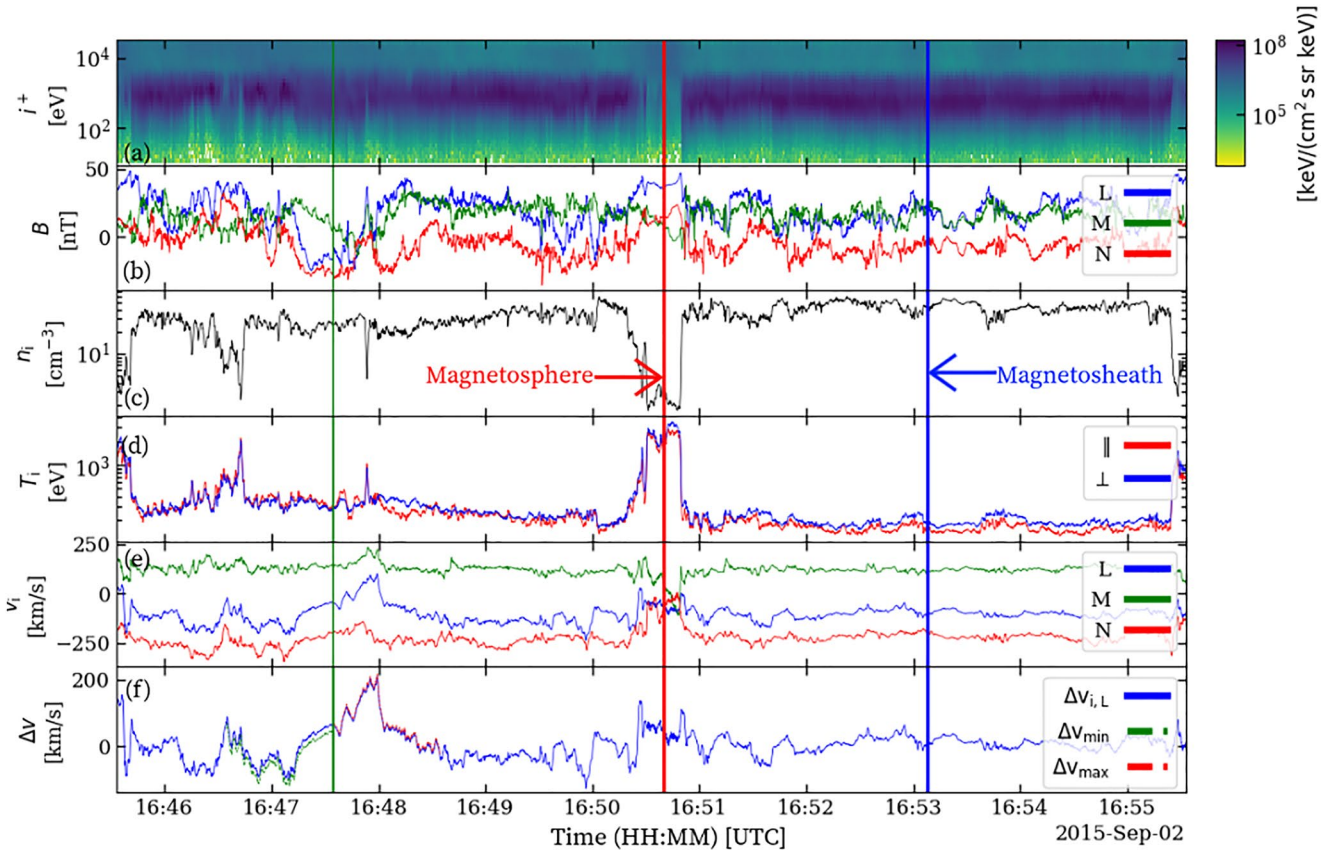

Figure 2. Time series of various data from Magnetospheric Multiscale (MMS) spacecraft. Top panel shows the ion energy spectra whereas the next panel (panel b) shows the time series of three magnetic field components in the LMN-coordinate system. Panels c and d show the ion density and temperatures. Panel e shows the ion velocity components. Vertical red and blue lines mark the location of magnetosphere and magnetosheath, as identified by the automated code. The last panel shows ΔV_L, which is the difference between V_L and the average value of V_L in the magnetosheath. The green vertical line shows the location of a jet, which is at the center point between the maximum and minimum value of ΔV_L.

$$\Delta V_L = V_L - \langle V_{L,sheath} \rangle \quad (5)$$

where $\langle V_{L,sheath} \rangle$ is the average value of L-component of ion velocity in the longest magnetosheath interval in the 10-min period and V_L is the time series data of the L-component of the ion velocity. We use this velocity, ΔV_L, to check for the presence of jet-reversal during crossings. In order to identify jet-reversal, we look for switches in ΔV_L by more than ±70 km/s within a 2-min window of the 10-min time series data. Previous studies (Petrinec et al., 2022; Trattner, Burch, et al., 2017) have used the same velocity change and time window values for a similar data set. This study adds additional conditions to the crossings in order to constrain uncertain crossing measurements. To remove artificial peaks, the algorithm only identifies a velocity switch as a jet-reversal if ΔV_L is larger (and smaller) than +70 km/s (−70 km/s) continuously for at least a time interval of 3 s. Once we find such a time interval, we check if the maximum and minimum values of ΔV_L occurred within a 2 min time interval of each other. Once that condition has been satisfied, we assign the time of the jet (t_{jet}) as the time between the maximum and minimum value of ΔV_L. If there are multiple instances of $|\Delta V_L| > 70$ km/s within the 10 min period, then the interval which has the highest peak of ΔV_L is checked for the presence of a jet. The methodology to identify jet reversals is based on the methodology developed by Trattner, Burch, et al. (2017) and used in previous statistical studies (Petrinec et al., 2022; Trattner, Burch, et al., 2017).

Figure 2 shows a typical MMS time series data of the parameters used in this study. The top panel (panel a) shows the ion energy spectra, and the next panel shows the magnetic field strength in the local LMN-coordinate system. Panels (c) and (d) show the ion-density and parallel and perpendicular temperatures, respectively. The dip in ion-density and the corresponding enhancement of ion temperature around 16:50:30 UTC, along with the change in ion-density spectra, is the indication of spacecraft moving from magnetosheath to magnetosphere. Next, panel (e) shows the time series of ion velocity components. Vertical red and blue lines mark the location of reference magne-

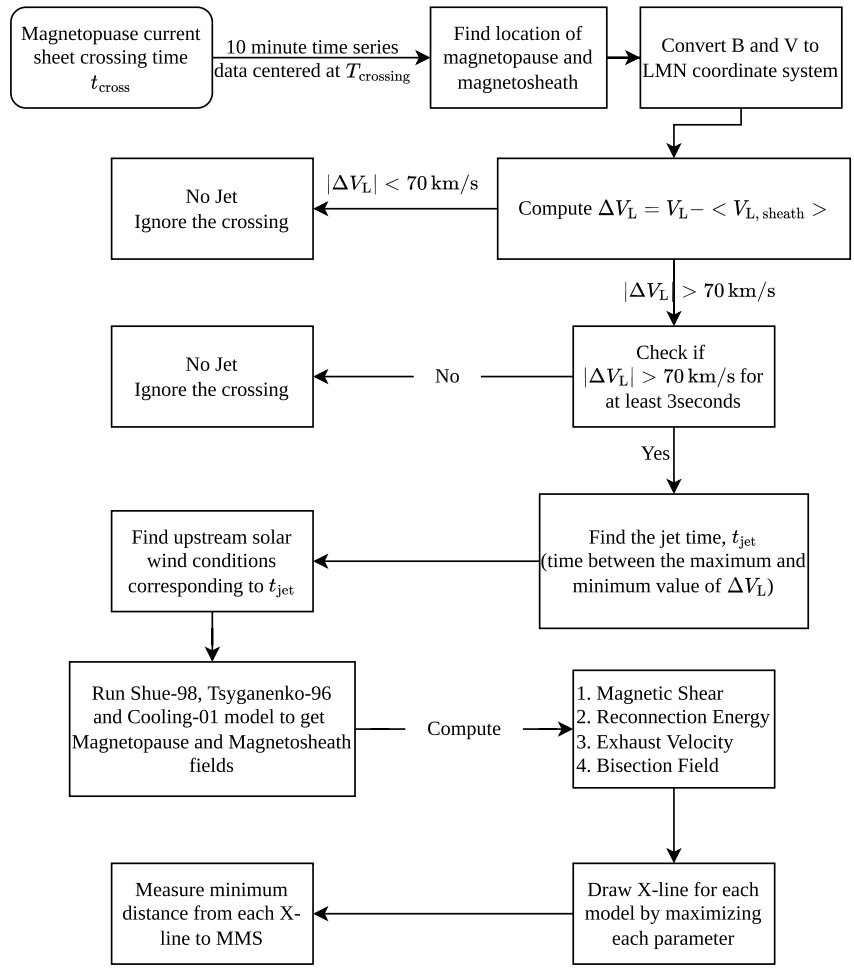

Figure 3. Flowchart of the algorithm used to select Magnetospheric Multiscale (MMS) magnetopause crossings for jet reversals and comparison to model X-line positions. See text for definition of each term and more details.

tosphere and magnetosheath, as identified by the automated code described earlier. The last panel (f) shows ΔV_L, which is the difference between V_L and the average value of V_L in the magnetosheath, described by Equation 5. The green vertical line shows the location of the center of the jet, which is at the center point between the maximum and minimum value of ΔV_L. The timestamp corresponding to this center point is referred as the time of the jet, t_{jet}.

Once a jet has been identified, a 10-min average value of solar wind observations from OMNI data centered at t_{jet} are used for the upstream condition. These solar wind upstream conditions are then used as input for the Shue-98 (Shue et al., 1998) model to compute the stand-off distance of the magnetopause subsolar point and the general shape of the magnetopause. The upstream solar wind conditions are then used with the output of the Shue-98 model as input for the Tsyganenko-96 (Tsyganenko, 1996) model, which provides the magnetic field at the magnetopause.

For the magnetosheath fields, we use the Cooling-01 (Cooling et al., 2001) model to obtain the draped magnetosheath field just outside the magnetopause. For the Cooling-01 model, the magnetosheath density is derived from MMS data (using the average observed value, as previously described) and for the magnetopause ion density we assume a standard density of 0.1 cm^{-3}. The output from these models is used to compute the value of four parameters (magnetic shear, reconnection energy, exhaust velocity and bisection field) over the magnetopause spread over a circular region of radius 20 R_E as described by Equations 1–4.

Next, to trace the location of the predicted reconnection line from each model, maximization of each of the respective parameters (except for Maximum Bisection Model, see Section 2.4) is carried out over the projected circular region along the draped field lines. Thereafter, we compute the minimum 3D distance of MMS spacecraft from each of the predicted line positions and store the value of distance to make statistical observations. Figure 3

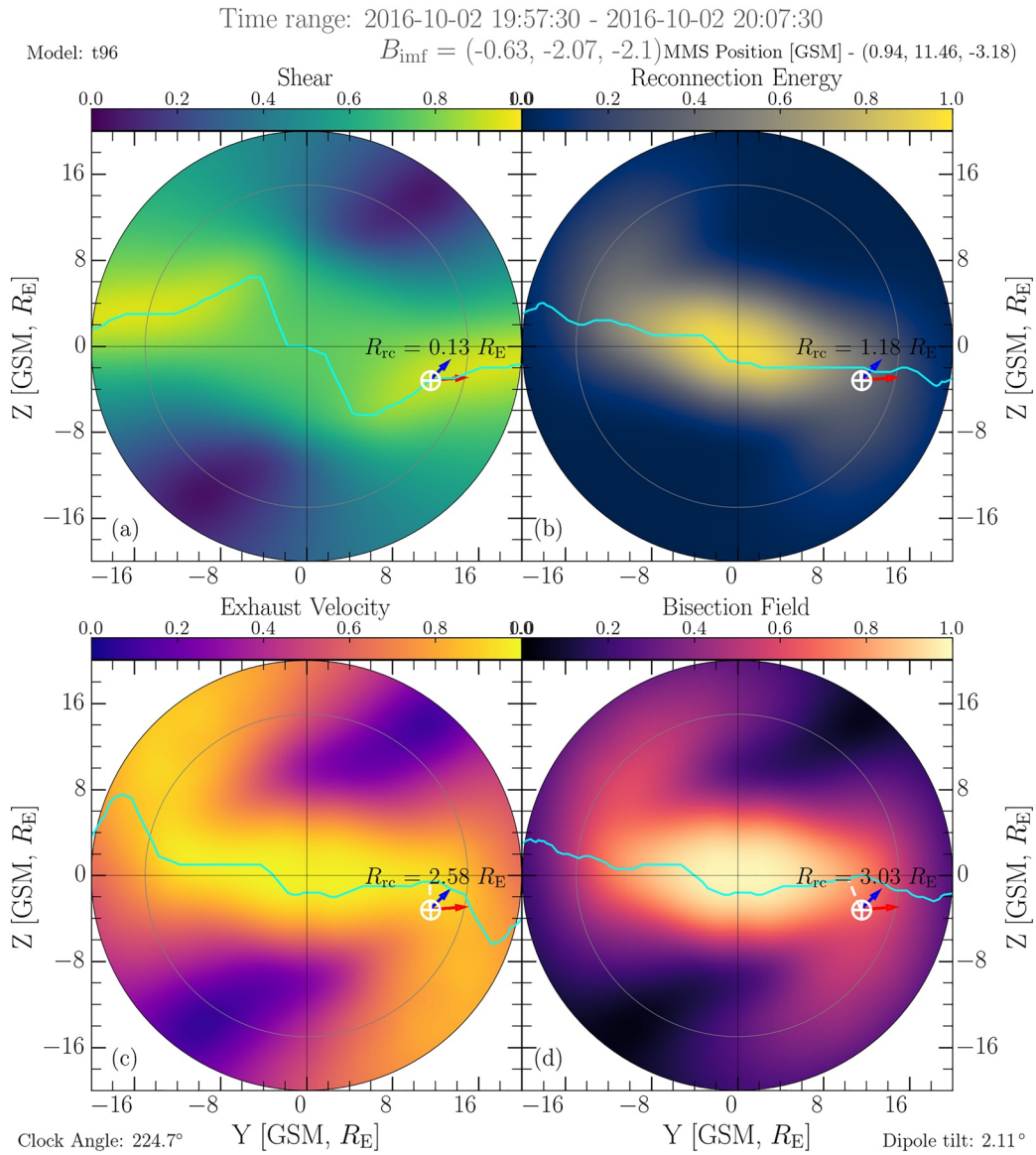

Figure 4. Location of reconnection line, cyan color, from four different models. Magnetospheric Multiscale (MMS) is represented by the white encircled plus. The red arrow shows the direction of the local magnetosheath field whereas the blue arrow shows the direction of the local ion velocity. R_{rc} is the measured minimum distance between the reconnection line and the spacecraft.

shows a flowchart of the algorithm described above. Figure 4 shows a typical case where we have plotted each of the four parameters on the *yz*-plane along the magnetopause along with the predicted X-line. The panels from a to d show shear, reconnection energy, exhaust velocity and bisection field. Each of these parameters are normalized against their maximum value in the plane so that they all range from 0 to 1. The gray circle at about 15 R_E corresponds to the terminator. MMS is represented by the white encircled plus. The red and blue arrow in each panel show the direction of the local magnetosheath field and ion velocity at the position of MMS. R_{rc} is the measured minimum 3D distance between the reconnection line and the spacecraft. For this study, cases where the point of minimum distance was outside the terminator were not used for the statistics.

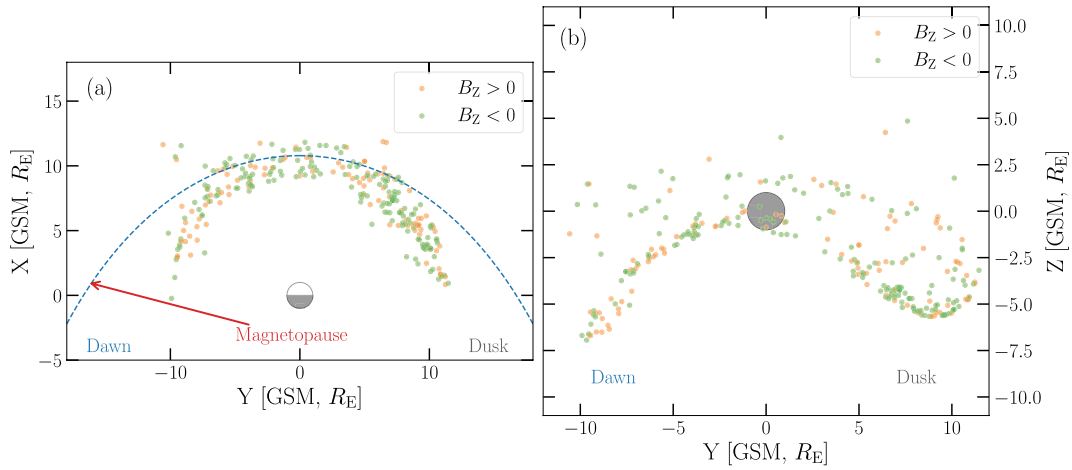

Figure 5. Location of all the reconnection events used in this study, as observed by Magnetospheric Multiscale (MMS), with nominal magnetopause shown as a dashed-blue line.

4. Results and Discussions

Using the methodology described in Section 3.2, between September 2015 and April 2018, a total of 274 jet reversals were identified. For each of these events, we computed the distance between the predicted X-line location and the MMS spacecraft. Figure 5 shows the location of each of the jets in *xy*-plane and *yz*-plane with a nominal magnetopause location shown by the dashed-blue line. The two colors represent jet-reversal detection corresponding to the directions of B_z (southward for green and northward for orange). The quantile values of various solar wind parameters corresponding to the time of observation of each event are listed in Table 2. These values are very similar to nominal solar wind conditions observed at 1 AU by the WIND spacecraft (Wilson et al., 2021). However, though the median value of B_z in the solar wind is very close to zero, for the 274 jet reversals observed, the average value of B_z in the solar wind was close to −1, which shows a bias for jet-reversal detection during southward IMF. This is to be expected because reconnection near the subsolar region is more common during southward IMF. Statistically, we found that we were twice as likely to find a jet-reversal during southward IMF compared to northward IMF. Figure 6 shows a histogram of the distance of the modeled reconnection X-line (R_{rc}) from the MMS spacecraft. The distance is plotted along the *x* axis in the units of Earth radius (R_E), with the frequency of events along *y* axis. The dashed line in each panel corresponds to the mean value of the histogram.

The performance of the models across the various solar wind conditions are now compared. The average value of distance between spacecraft and the predicted X-line for Maximum Bisection Field Model and Maximum Reconnection Energy Model are similar, though the Maximum Bisection Field Model with an average measured distance of 4.22 R_E has the lowest value among the four tested models (see Table 3). The histogram for Maximum Bisection Field Model also has the least spread (see Figure 6), implying the precision of the model, however it seems to lack the accuracy of the Maximum Shear Model under some conditions (discussed later in this section). The precision of the Maximum Bisection Field Model can be explained, in part, by the inherent observational bias in the data. Most of the jet reversals were observed by MMS in the equatorial plane, very close to the subsolar point (see Figure 5). In addition, for most upstream conditions (except for conditions with positive B_x), the Maximum Bisection Field Model tends to predict the X-line location along or close to the equator; it therefore makes sense that the spread for this model will be least compared to other models.

Table 2
Average Values of Solar Wind Parameters During Observed Jet Reversals

	Percentile		
Parameter	5th	50th	95th
|**B**| (nT)	2.69	4.76	9.67
n_i (cm^{-3})	2.22	4.97	12.02
P_{dyn} (nPa)	1.23	2.23	4.88
V_i (km/s)	337	507	693
T_i (ev)	2.55	10.20	27.89

Under the condition $B_z < 0$, the accuracy of each model improves compared to all IMF conditions. Figure 7 shows the histogram corresponding to this condition and Table 3 shows the difference in average values corresponding to two different conditions ($B_z > 0$ and $B_z < 0$) along with the average value of measured reconnection distance for each model for three different conditions. The improvement is most significant in the case of Maximum Reconnection Energy Model where the average value changes by 3.15 R_E followed by Maximum Exhaust Velocity Model (a change of 2.53 R_E). The correlation between

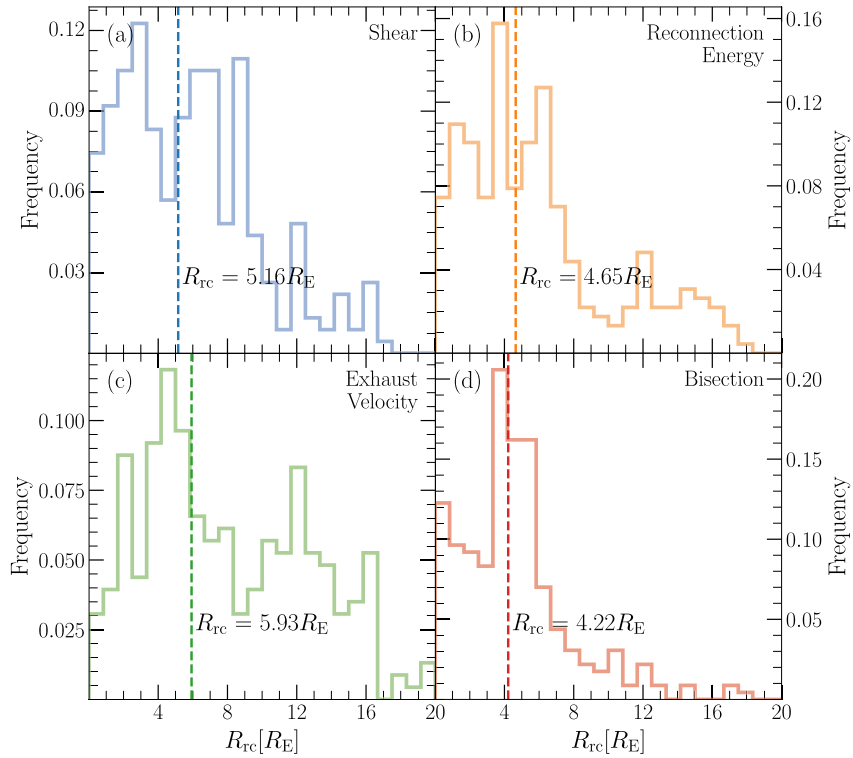

Figure 6. A histogram of the shortest distance between the Magnetospheric Multiscale (MMS) spacecraft and the predicted X-line location for different models. The distance is plotted along the *x* axis in units of the Earth radius, with counts along *y* axis. The vertical dashed line in each panel corresponds to the mean distance of 274 individual measurements.

the model accuracy and the value of B_z can also be seen in Figure 8. Figure 8 shows the highest value of Pearson correlation coefficient for Maximum Reconnection Energy Model and Maximum Exhaust Velocity Model implying greater dependency of the accuracy of these two models on B_z followed by Maximum Shear Model and Maximum Bisection Field Model, which understandably shows the least correlation between the two parameters. For Figure 8, the histogram along each axis shows the distribution of the associated parameter.

Figure 9 shows the distribution between the cone angle ($\theta_{cone} = \cos^{-1}(B_x/|\mathbf{B}|)$) and the z component of IMF. Low θ_{cone} means the IMF is dominated by the radial magnetic field component and likely has a foreshock upstream of the dayside magnetopause. Each bubble represents an observation point and its radius is proportional to the measured distance between X-line and MMS for the corresponding model. The larger bubble implies lesser accuracy in predicting the location of X-line by the model. For both the Maximum Bisection Field Model and Maximum Reconnection Energy Model at $B_z > 0$ there is a visible increment in R_{rc} values (see Table 3). At all θ_{cone}, as long as B_z is negative, these two models remain fairly accurate. For midrange values of θ_{cone} (values between [50, 120] degrees), for all values of B_z, the model (Maximum Bisection Field Model and Maximum Reconnection

Table 3
Table of Average Distance Between MMS Observation and Model Predicted X-Line Locations for Different Conditions of z Component of IMF B_z

Model	Average distance (R_{rc})			
	All IMF conditions	$\langle R_{rc,B_z<0} \rangle$	$\langle R_{rc,B_z>0} \rangle$	Difference, $\Delta R_rc(\langle R_{rc,B_z>0} \rangle - \langle R_{rc,B_z<0} \rangle)$
Maximum Shear Model	5.16	4.53	6.34	1.81
Maximum Reconnection Energy Model	4.65	3.74	6.88	3.14
Maximum Exhaust Velocity Model	5.93	5.16	7.69	2.53
Maximum Bisection Field Model	4.22	3.65	5.27	1.62

Note. $\langle R_{c,B_z<0} \rangle$ refers to average distance from reconnection line for cases where $B_Z < 0$.

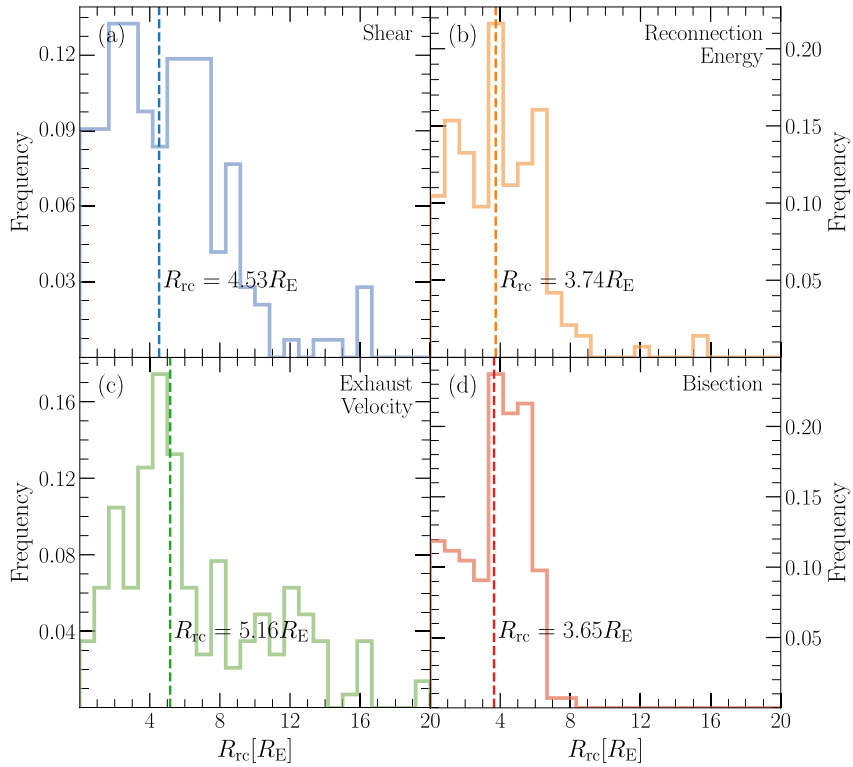

Figure 7. A histogram of the shortest distance between the Magnetospheric Multiscale (MMS) spacecraft and the predicted X-line location for different models when $B_z < 0$. The distance is plotted along the x axis in units of the Earth radius, with counts along y axis. The vertical dashed line in each panel corresponds to the mean distance.

Energy Model) predictions remain accurate. The Maximum Shear Model performs similarly but with two interesting differences. For midrange values of cone angle, for all values of B_z and especially for positive values, the Maximum Shear Model does the best job of predicting the correct location of X-line. And at low values of the cone angle, the Maximum Shear Model performs as well as the Maximum Reconnection Energy and Maximum Bisection Field Models. At very high values of θ_{cone} (>150°) irrespective of the sign of B_z, the Maximum Shear Model performs relatively poorly ($\langle R_{c,shear} \rangle = 9.50\ R_E$ versus $\langle R_{c,bisec} \rangle = 3.65\ R_E$).

In Figure 9, there is also an asymmetry in the computed values of R_{rc} for very low ($\theta_{cone} < 30°$) and very high ($\theta_{cone} > 150°$) cone angles for all models. This can in part be explained the fact that the effect on the draping filed, as computed using the Cooling-01 model, is not symmetric for positive and negative B_x. Also, while computing the fields using the T-96 model, the dipole tilt of the Earth is considered whereas it is ignored during computation of the draping field using the Cooling-01 model. This also leads to some asymmetry to the result of computed distance. Though this asymmetry is present in all cases, it is most pronounced for the Maximum Shear Model. Previous work has reported that the Maximum Shear Model was less accurate during time periods with large B_x or small θ_{cone} possibly due to the draping model being used (Trattner, Thresher, et al., 2017).

In order to look at the affect of B_y on the accuracy of the models, we plot $B_y/|\mathbf{B}|$ against the z component of IMF in Figure 10. Figure 10 is made in a similar style to that of Figure 9, except that $B_y/|\mathbf{B}|$ is along the y axis. We plot this ratio instead of the value of B_y in order to look at the variation in different X-line predictions based on how dominant the y component is. It has been noted in the literature (Trattner, Thresher, et al., 2017) that for dominant B_y the Maximum Shear Model still works even for a northward IMF. We find that to be the case here as well in the top left panel of Figure 10 corresponding to the Maximum Shear Model. For the other models shown in Figure 10, the effects of B_y are much less prominent. This is clear from Table 4 where we have shown the average values of R_c corresponding to cases $B_y/|\mathbf{B}| > 0.8$ (dominant B_y) and $B_y/|\mathbf{B}| < 0.3$ as well as the percentage change in the average values for all four models. The Maximum Shear Model has the highest change percentage whereas the Maximum Bisection Field Model is least affected by the change in $B_y/|\mathbf{B}|$. The effect of B_y is even more dominant when we only consider the cases where the IMF was northward. In such conditions, the accuracy of the Maximum Shear Model increases by ~45%.

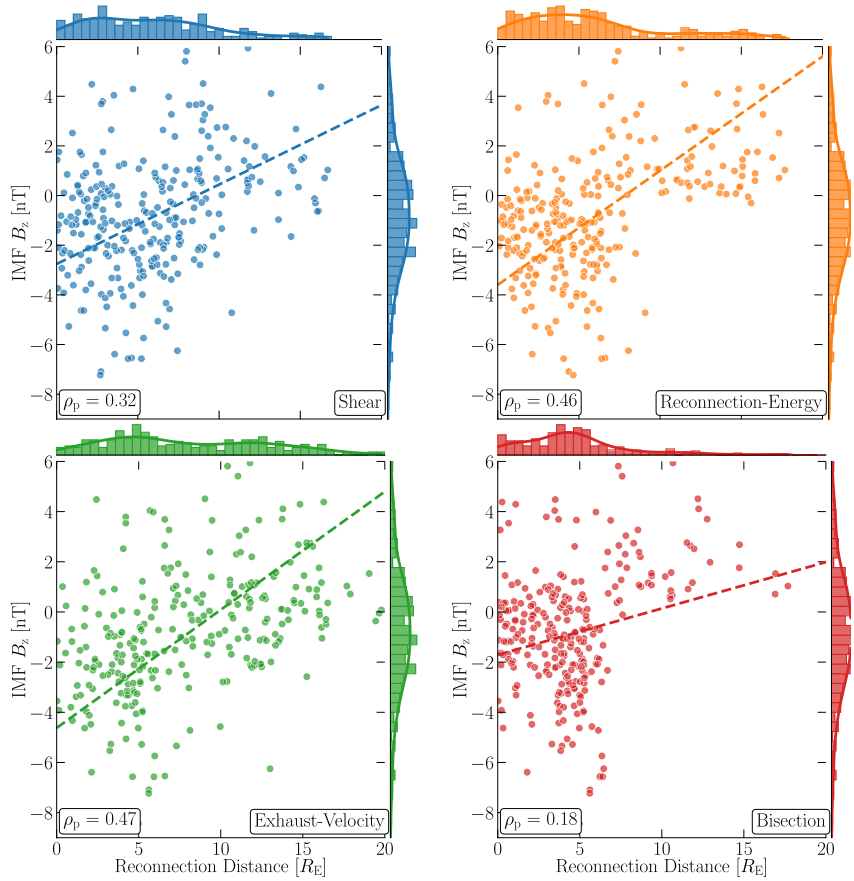

Figure 8. Correlation between the z component of the interplanetary magnetic field (IMF) and the distance between the predicted X-line and Magnetospheric Multiscale (MMS) for different models. ρ_p is the Pearson correlation coefficient. The dashed lined is the trend line with ρ_p as slope. The histogram along the edges shows the distribution of parameters.

The Maximum Exhaust Velocity Model performs worst compared to all the other models in this study. Although there is significant improvement in the prediction accuracy when we consider cases of only negative B_z (see Table 3), the average R_{rc} values are greater than those of all other models. Part of the reason for this poor performance might be the fact that the Maximum Exhaust Velocity Model uses both the magnetic field and density of ions in its computation of the hybrid Alfvén speed. We explicitly assume the value of ion density in the magnetosphere to be 0.1 cm^{-3} which would have an impact on the accuracy of the computed velocity.

5. Summary and Conclusion

Magnetic reconnection occurring at the magnetopause of Earth is known to exert a significant influence on magnetospheric convection and facilitates the influx of mass and energy into the magnetosphere/ionosphere system. Despite its importance, the factors governing the location of a dayside magnetic reconnecting X-line are not well understood. Several models have been proposed to predict the location of the X-line. For this study, we chose to compare the statistical performance of four such models. These models share a common assumption that the X-line location can be determined by the maximization of a physical quantity along the magnetopause boundary. The models considered maximizes the magnetic shear, magnetic reconnection energy, hybrid exhaust velocity and the bisection field. We referred to them as Maximum Shear Model, Maximum Reconnection Energy Model, Maximum Exhaust Velocity Model, and Maximum Bisection Field Model.

We report the performance of these models under various upstream solar wind conditions. We used high cadence MMS data in conjunction with data from OMNI. Output from models (Tsyganenko-96, Shue-98, and Cooling-01) was used to get the magnetospheric and magnetosheath magnetic fields. In order to locate the actual locations of the X-line, we found the time intervals where MMS observed jet reversals with sustained high positive and negative values of ion velocities for at least 3 s in each direction, within a 2 min window. The location of MMS at these

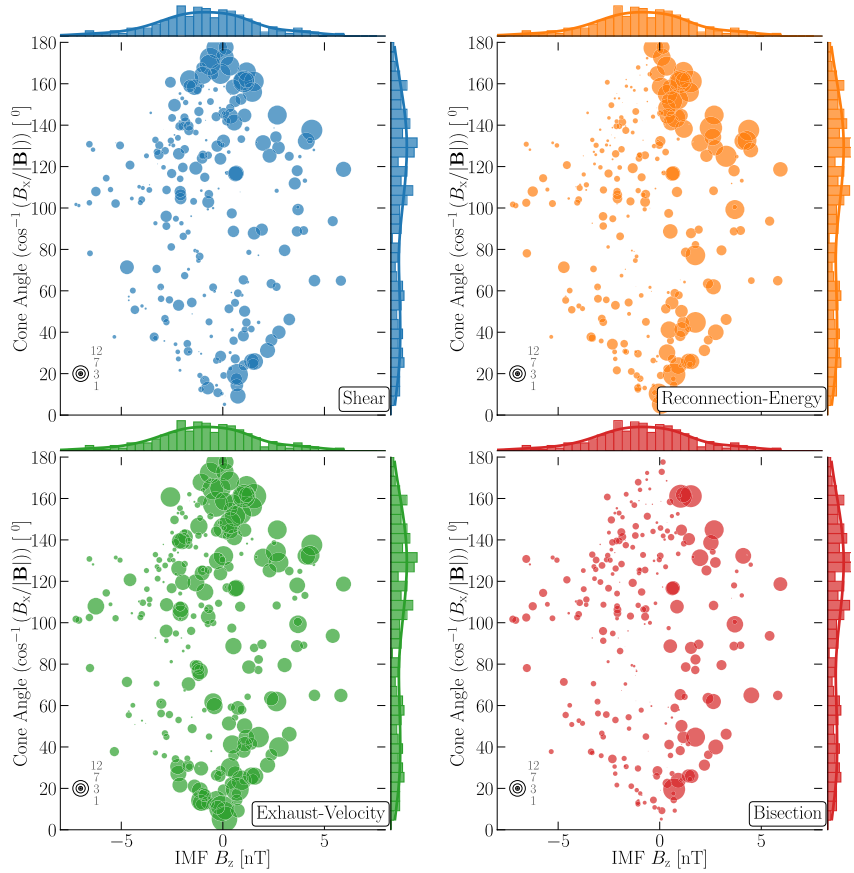

Figure 9. Plot between the interplanetary magnetic field (IMF) cone angle and the corresponding z component for different models. The size of each circular marker is a representative of measured reconnection distance from the predicted X-line location. Histograms on each of the axes represent the distribution of the parameter along those axes.

intervals was then compared with the prediction for an X-line from the aforementioned four different models. We computed the shortest distance between the predicted X-line and the MMS location. For the 274 jet reversals observed between September 2015 and April 2018, under no constraints on the upstream IMF conditions, the Maximum Bisection Field Model gives the shortest average distance from the estimated X-line compared to the other models with an average value of $R_{rc} = 4.22\ R_E$. The Maximum Reconnection Energy Model does a comparable job with an average value of $R_{rc} = 4.65\ R_E$. For the cases where $B_z < 0$, we observe maximum improvement for the Maximum Reconnection Energy ($R_{rc} = 3.74\ R_E$) thereby implying strongest dependence on B_z. Though for the Maximum Bisection Field Model, the improvement is not as significant ($R_{rc} = 3.65\ R_E$), it still is the best model. Under most circumstances, we found that the Maximum Bisection Model performed best.

Considering the effect of B_y, we reconfirmed the results of (Trattner, Thresher, et al., 2017), that for a dominant B_y, ($B_y/|\mathbf{B}| > 0.8$), the Maximum Shear Model performs well, at par with the Maximum Reconnection Energy Model and slightly worse than the Maximum Bisection Field Model. The difference in the improvement of the Maximum Shear Model was highest (~28%) for the four tested models. If we consider dominant B_y along with $B_z > 0$, the improvement in the mean distance predicted by the model increases to ~45%.

Overall, the Maximum Bisection Field Model seems to perform best for different upstream conditions and also appears to be most precise. However, part of the reason for this can be attributed to the inherent observational bias in the MMS data. The Maximum Bisection Field Model tends to predict the location of X-line along or close to the equator, which is also where MMS observed most of the jet reversals (see Figure 5).

Among the four models we compared and various solar wind conditions that we observed, the Maximum Exhaust Velocity Model seems to perform poorest. This can partly be because in this study we assumed the magnetospheric ion density to be constant ($n_i = 0.1\ \text{cm}^{-3}$) which is not necessarily true. An accurate measurement of the density would alter the hybrid Alfvén velocity and thus affect the average values of measured distance.

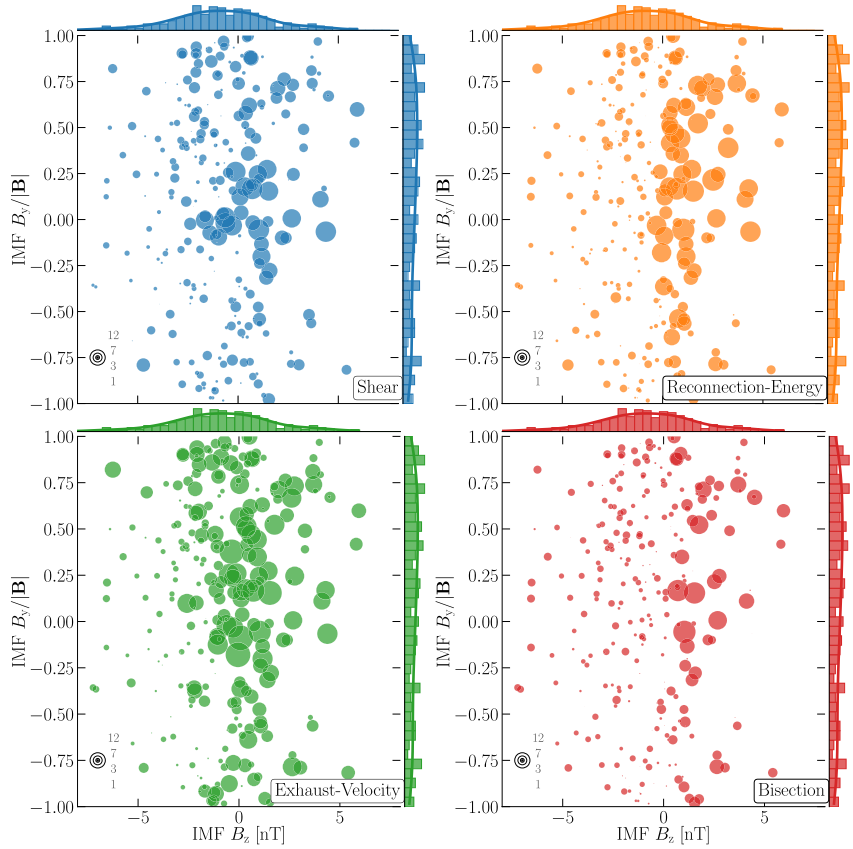

Figure 10. Plot between the ratio of interplanetary magnetic field (IMF) y component to its magnitude and corresponding z component for different models. The size of each circular marker is a representative of measured reconnection distance from the predicted X-line location. Histograms on each of the axes represent the distribution of the parameter along those axes.

Though, as expected, the accuracy of all the models improves with the strength of southwards IMF, the effect is most pronounced for Maximum Exhaust Velocity Model and least for the Maximum Bisection Field Model as seen in Figure 8. The Maximum Exhaust Velocity Model is also most affected by the extreme values of the cone angle (<30° and >150°). Though for small cone angles, and for southward oriented IMF, the Maximum Shear Model is fairly accurate, at high values of cone angle, for all B_z, the model tends to perform poorly, as seen in Figure 9. For this condition, however, the Maximum Reconnection Energy and the Maximum Bisection Field Model remain largely unaffected.

Table 4
Table of Average Distance Between MMS Observation and Model Predicted X-Line Locations for Different Values of IMF $B_y/|\mathbf{B}|$

	Average distance (R_E)		Difference, ΔR_{rc}
Model	$B_y/\|\mathbf{B}\| < 0.3$	$B_y/\|\mathbf{B}\| > 0.8$	(Percentage)
Maximum Shear Model	7.57	5.48	27.61
Maximum Reconnection Energy Model	6.79	5.45	19.73
Maximum Exhaust Velocity Model	8.98	7.95	11.47
Maximum Bisection Field Model	4.82	4.69	2.70

Data Availability Statement

MMS data used in this study are available from the MMS Science Data Center (https://lasp.colorado.edu/mms/sdc/public/about) and the OMNI data are available at the OMNI data center (https://omniweb.gsfc.nasa.gov/ow.html). The codes used to analyze the data and generate the figures in this study are published on GitHub under the GNU General Public License (https://github.com/qudsiramiz/rxn_location) (Qudsi, 2023).

Acknowledgments
The authors would like to thank Dr. Karl-heinz Trattner and Dr. Steven Petrinec for their valuable discussions on data and for clarifications provided on the implementation and limitations of Maximum Shear Model. This study was funded by NASA grant 80NSSC20K1356.

References

Cassak, P. A., & Fuselier, S. A. (2016). Reconnection at earth's dayside magnetopause. In *Magnetic reconnection* (pp. 213–276). Springer International Publishing. https://doi.org/10.1007/978-3-319-26432-5_6

Cassak, P. A., & Shay, M. A. (2007). Scaling of asymmetric magnetic reconnection: General theory and collisional simulations. *Physics of Plasmas*, *14*(10), 102114. https://doi.org/10.1063/1.2795630

Cooling, B. M. A., Owen, C. J., & Schwartz, S. J. (2001). Role of the magnetosheath flow in determining the motion of open flux tubes. *Journal of Geophysical Research*, *106*(A9), 18763–18775. https://doi.org/10.1029/2000JA000455

Cowley, S. W. H. (1982). The causes of convection in the earth's magnetosphere: A review of developments during the IMS. *Reviews of Geophysics*, *20*(3), 531–565. https://doi.org/10.1029/RG020i003p00531

Crooker, N. U. (1979). Dayside merging and cusp geometry. *Journal of Geophysical Research*, *84*(A3), 951–959. https://doi.org/10.1029/JA084iA03p00951

Dungey, J. W. (1961). Interplanetary magnetic field and the auroral zones. *Physical Review Letters*, *6*(2), 47–48. https://doi.org/10.1103/physrevlett.6.47

Dunlop, M. W., Zhang, Q.-H., Bogdanova, Y. V., Trattner, K. J., Pu, Z., Hasegawa, H., et al. (2011). Magnetopause reconnection across wide local time. *Annales Geophysicae*, *29*(9), 1683–1697. https://doi.org/10.5194/angeo-29-1683-2011

Fuselier, S. A., Lewis, W. S., Schiff, C., Ergun, R., Burch, J. L., Petrinec, S. M., & Trattner, K. J. (2014). Magnetospheric multiscale science mission profile and operations. *Space Science Reviews*, *199*(1–4), 77–103. https://doi.org/10.1007/s11214-014-0087-x

Fuselier, S. A., Trattner, K. J., & Petrinec, S. M. (2011). Antiparallel and component reconnection at the dayside magnetopause. *Journal of Geophysical Research*, *116*, A10227. https://doi.org/10.1029/2011JA016888

Fuselier, S. A., Vines, S. K., Burch, J. L., Petrinec, S. M., Trattner, K. J., Cassak, P. A., et al. (2017). Large-scale characteristics of reconnection diffusion regions and associated magnetopause crossings observed by MMS. *Journal of Geophysical Research: Space Physics*, *122*, 5466–5486. https://doi.org/10.1002/2017JA024024

Gonzalez, W. D., & Mozer, F. S. (1974). A quantitative model for the potential resulting from reconnection with an arbitrary interplanetary magnetic field. *Journal of Geophysical Research*, *79*(28), 4186–4194. https://doi.org/10.1029/JA079i028p04186

Gosling, J. T., Asbridge, J. R., Bame, S. J., Feldman, W. C., Paschmann, G., Sckopke, N., & Russell, C. T. (1982). Evidence for quasi-stationary reconnection at the dayside magnetopause. *Journal of Geophysical Research*, *87*(A4), 2147–2158. https://doi.org/10.1029/JA087iA04p02147

Grimes, E. W., Hatzigeorgiu, N., Lewis, J. W., Russell, C., McTiernan, J. M., Drozdov, A., & Angelopoulos, V. (2019). pySPEDAS: Space physics environment data analysis Software in Python. In *Abstract SH41C-3313 Presented at 2019 Fall Meeting*. American Geophysical Union.

Haaland, S., Paschmann, G., Øieroset, M., Phan, T., Hasegawa, H., Fuselier, S. A., et al. (2020). Characteristics of the Flank magnetopause: MMS results. *Journal of Geophysical Research: Space Physics*, *125*, e27623. https://doi.org/10.1029/2019JA027623

Hesse, M., Aunai, N., Zenitani, S., Kuznetsova, M., & Birn, J. (2013). Aspects of collisionless magnetic reconnection in asymmetric systems. *Physics of Plasmas*, *20*(6), 061210. https://doi.org/10.1063/1.4811467

King, J. H., & Papitashvili, N. E. (2005). Solar wind spatial scales in and comparisons of hourly wind and ace plasma and magnetic field data. *Journal of Geophysical Research*, *110*, A02104. https://doi.org/10.1029/2004JA010649

Komar, C. M., Fermo, R. L., & Cassak, P. A. (2015). Comparative analysis of dayside magnetic reconnection models in global magnetosphere simulations. *Journal of Geophysical Research: Space Physics*, *120*, 276–294. https://doi.org/10.1002/2014JA020587

Liu, Y.-H., Hesse, M., Li, T. C., Kuznetsova, M., & Le, A. (2018). Orientation and stability of asymmetric magnetic reconnection x line. *Journal of Geophysical Research: Space Physics*, *123*, 4908–4920. https://doi.org/10.1029/2018JA025410

Moore, T. E. (2002). The dayside reconnection x line. *Journal of Geophysical Research*, *107*(A10), 1332. https://doi.org/10.1029/2002JA009381

Muzamil, F. M., Farrugia, C. J., Torbert, R. B., Pritchett, P. R., Mozer, F. S., Scudder, J. D., et al. (2014). Structure of a reconnection layer poleward of the cusp: Extreme density asymmetry and a guide field. *Journal of Geophysical Research: Space Physics*, *119*, 7343–7362. https://doi.org/10.1002/2014JA019879

Paschmann, G. (2008). Recent in-situ observations of magnetic reconnection in near-earth space. *Geophysical Research Letters*, *35*, L19109. https://doi.org/10.1029/2008GL035297

Paschmann, G., Haaland, S. E., Phan, T. D., Sonnerup, B. U. O., Burch, J. L., Torbert, R. B., et al. (2018). Large-scale survey of the structure of the dayside magnetopause by MMS. *Journal of Geophysical Research: Space Physics*, *123*, 2018–2033. https://doi.org/10.1002/2017JA025121

Paschmann, G., Øieroset, M., & Phan, T. (2013). In-situ observations of reconnection in space. *Space Science Reviews*, *178*(2–4), 385–417. https://doi.org/10.1007/s11214-012-9957-2

Paschmann, G., Papamastorakis, I., Baumjohann, W., Sckopke, N., Carlson, C. W., Sonnerup, B. U. O., & Lühr, H. (1986). The magnetopause for large magnetic shear: AMPTE/IRM observations. *Journal of Geophysical Research*, *91*(A10), 11099–11115. https://doi.org/10.1029/JA091iA10p11099

Paschmann, G., Sonnerup, B. U., Papamastorakis, I., Sckopke, N., Haerendel, G., Bame, S. J., et al. (1979). Plasma acceleration at the earth's magnetopause: Evidence for reconnection. *Nature*, *282*(5736), 243–246. https://doi.org/10.1038/282243a0

Petrinec, S. M., Burch, J. L., Fuselier, S. A., Trattner, K. J., Giles, B. L., & Strangeway, R. J. (2022). On the occurrence of magnetic reconnection along the terrestrial magnetopause, using magnetospheric multiscale (MMS) observations in proximity to the reconnection site. *Journal of Geophysical Research: Space Physics*, *127*, e2021JA029669. https://doi.org/10.1029/2021JA029669

Pollock, C., Moore, T., Jacques, A., Burch, J., Gliese, U., Saito, Y., et al. (2016). Fast plasma investigation for magnetospheric multiscale. *Space Science Reb views*, *199*(1–4), 331–406. https://doi.org/10.1007/s11214-016-0245-4

Pu, Z. Y., Zhang, X. G., Wang, X. G., Wang, J., Zhou, X.-Z., Dunlop, M. W., et al. (2007). Global view of dayside magnetic reconnection with the dusk-dawn IMF orientation: A statistical study for double star and cluster data. *Geophysical Research Letters*, *34*, L20101. https://doi.org/10.1029/2007GL030336

Qudsi, R. (2023). qudsiramiz/rxn_location: V0.1.1 [Dataset]. Zenodo. https://doi.org/10.5281/zenodo.8187212

Russell, C. T., Anderson, B. J., Baumjohann, W., Bromund, K. R., Dearborn, D., Fischer, D., et al. (2016). The magnetospheric multiscale magnetometers. *Space Science Reviews*, *199*(1–4), 189–256. https://doi.org/10.1007/s11214-014-0057-3

Shue, J.-H., Song, P., Russell, C. T., Steinberg, J. T., Chao, J. K., Zastenker, G., et al. (1998). Magnetopause location under extreme solar wind conditions. *Journal of Geophysical Research*, *103*(A8), 17691–17700. https://doi.org/10.1029/98JA01103

Souza, V. M., Gonzalez, W. D., Sibeck, D. G., Koga, D., Walsh, B. M., & Mendes, O. (2017). Comparative study of three reconnection x line models at the earth's dayside magnetopause using in situ observations. *Journal of Geophysical Research: Space Physics*, *122*, 4228–4250. https://doi.org/10.1002/2016JA023790

Torbert, R. B., Russell, C. T., Magnes, W., Ergun, R. E., Lindqvist, P. A., Le Contel, O., et al. (2016). The FIELDS instrument suite on MMS: Scientific objectives, measurements, and data products. *Space Science Reviews*, *199*(1–4), 105–135. https://doi.org/10.1007/s11214-014-0109-8

Trattner, K. J., Burch, J. L., Ergun, R., Eriksson, S., Fuselier, S. A., Giles, B. L., et al. (2017). The MMS dayside magnetic reconnection locations during phase 1 and their relation to the predictions of the maximum magnetic shear model. *Journal of Geophysical Research: Space Physics*, *122*, 11991–12005. https://doi.org/10.1002/2017JA024488

Trattner, K. J., Mulcock, J. S., Petrinec, S. M., & Fuselier, S. A. (2007). Probing the boundary between antiparallel and component reconnection during southward interplanetary magnetic field conditions. *Journal of Geophysical Research*, *112*, A08210. https://doi.org/10.1029/2007JA012270

Trattner, K. J., Petrinec, S. M., & Fuselier, S. A. (2021). The location of magnetic reconnection at earth's magnetopause. *Space Science Reviews*, *217*(3), 41. https://doi.org/10.1007/s11214-021-00817-8

Trattner, K. J., Thresher, S., Trenchi, L., Fuselier, S. A., Petrinec, S. M., Peterson, W. K., & Marcucci, M. F. (2017). On the occurrence of magnetic reconnection equatorward of the cusps at the Earth's magnetopause during northward IMF conditions. *Journal of Geophysical Research: Space Physics*, *122*, 605–617. https://doi.org/10.1002/2016JA023398

Tsyganenko, N. A. (1996). Effects of the solar wind conditions in the global magnetospheric configurations as deduced from data-based field models (invited). In E. J. Rolfe & B. Kaldeich (Eds.), *Proceedings of the international conference on substorms* (Vol. 389, p. 181). European Space Agency. Retrieved from https://ui.adsabs.harvard.edu/abs/1996ESASP.389..181T

Wilson, L. B., III, Brosius, A. L., Gopalswamy, N., Nieves-Chinchilla, T., Szabo, A., Hurley, K., et al. (2021). A quarter century of wind spacecraft discoveries. *Reviews of Geophysics*, *59*, e2020RG000714. https://doi.org/10.1029/2020RG000714